



Pergamon

Available online at www.sciencedirect.com

SCIENCE @ DIRECT®



Acta Materialia 51 (2003) 4803–4814

www.actamat-journals.com

Mechanical properties of Al(Sc,Zr) alloys at ambient and elevated temperatures

Christian B. Fuller, David N. Seidman, David C. Dunand *

Department of Materials Science and Engineering, Northwestern University, 2220 Campus Drive, Evanston, IL 60208-3108, USA

Received 27 May 2003; received in revised form 27 May 2003; accepted 5 June 2003

Abstract

This study investigates the mechanical properties of ternary Al(Sc,Zr) alloys containing 0.27–0.77 vol.% of $\text{Al}_3(\text{Sc,Zr})$ precipitates with an average radius $\langle r \rangle = 2\text{--}24$ nm. Microhardness values at ambient temperature follow predictions of the Orowan dislocation bypass mechanism, with a transition to the precipitate shearing mechanism predicted for $\langle r \rangle$ larger than 2 nm. Addition of Zr to binary Al(Sc) alloys delays the onset and kinetics of over-aging at 350 and 375 °C, but has little influence on the magnitude of the peak microhardness. Creep deformation at 300 °C is characterized by a threshold stress, which increases with $\langle r \rangle$ in the range 2–9 nm, in agreement with prior results for binary Al(Sc) alloys and a recently developed general climb model considering elastic interactions between dislocations and coherent, misfitting precipitates. At constant $\langle r \rangle$ and precipitate volume fraction, Zr additions do not significantly improve the creep resistance of Al(Sc) alloys.

© 2003 Acta Materialia Inc. Published by Elsevier Ltd. All rights reserved.

Keywords: Al–Sc–Zr alloys; Mechanical properties; Creep; Deformation mechanisms

1. Introduction

Precipitation-strengthened binary Al(Sc) alloys are usable up to 300 °C due to the presence of elastically hard and coherent Al_3Sc precipitates that form with an L1_2 -type crystal structure, a small lattice parameter misfit with Al (1.34% at 24 °C), a high melting temperature of 1320 °C, and a maximum solid solubility of 0.23 at.% Sc at the

eutectic temperature of 660 °C [1–3]. The presence of Al_3Sc precipitates has been shown to increase the creep resistance of coarse-grained binary Al(Sc) alloys [4–7]. In particular, Marquis et al. [5] examined the ambient- and elevated-temperature strengthening mechanisms of these alloys. Among possible ternary alloying elements, Zr is known to increase the strength as well as the recrystallization resistance of Al(Sc) alloys by substitution of Sc for Zr to form $\text{Al}_3(\text{Sc}_{1-x}\text{Zr}_x)$ precipitates with decreased coarsening kinetics (in comparison to the coarsening kinetics of Al_3Sc precipitates) [8–11].

Zirconium decreases the lattice parameter of $\text{Al}_3(\text{Sc}_{1-x}\text{Zr}_x)$, as observed experimentally by Refs.

* Corresponding author. Tel.: +1-847-491-5370; fax: +1-847-467-6573.

E-mail addresses: cfuller@rws.com (C.B. Fuller); d-seidman@northwestern.edu (D.N. Seidman); dunand@northwestern.edu (D.C. Dunand).

[3,12]. By changing the Sc/Zr ratio, it is therefore possible to tailor the lattice parameter mismatch between the $L1_2$ precipitates and the Al matrix. Relatively little research has been performed on the mechanical properties and deformation mechanisms of Al(Sc,Zr) alloys. Zirconium additions are known to increase the ambient temperature tensile strength and recrystallization resistance of Al(Sc) alloys [8,9,13,14]. Additions of Sc and Zr to commercial 2618 (Al–Cu–Mg–Fe–Ni), 5083 (Al–Mg–Mn), and 5754 (Al–Mg–Mn) aluminum alloys have been shown to increase the tensile strength over Zr-free alloys, an effect attributed to the pinning of grain- and subgrain-boundaries by highly stable $Al_3(Sc_{1-x}Zr_x)$ precipitates [15–17].

A fine-grained Al–Zn–Mg–Sc–Zr alloy was superplastically deformed at 420–500 °C to an elongation of 570–760% [9,18]. After superplastic deformation and aging (100 °C for 20 h followed by 170 °C for 5 h), this alloy exhibited ultimate tensile strengths (485–540 MPa) near those of the undeformed alloy. Superplastic deformation was also performed at 477 °C and a relatively high strain rate of $2 \times 10^{-3} \text{ s}^{-1}$, utilizing a series of Al–2.7 Mg–3.2 Zn–1.1 Cu (at.%) alloys with 0–0.2 at.% Sc and 0.006–0.04 at.% Zr [19]. The alloys containing only Sc or Zr (but not both) did not display superplastic behavior, which was attributed to the low number density of precipitates in the Zr-containing alloy and the low coarsening resistance in the Sc-containing alloy. Simultaneous additions of Sc and Zr, however, produced superplastic alloys with elongations between 556 and 668%. Finally, zirconium additions to polycrystalline specimens of the Al_3Sc intermetallic [20], forming an $Al_3(Sc_{0.74}Zr_{0.26})$ solid solution, were shown to decrease the strain rate at a given stress by nearly an order of magnitude as compared to binary Al_3Sc . The improved creep resistance was attributed to solid-solution strengthening by Zr atoms, which increases the stress necessary for dislocation motion.

This article reports on the effects of Zr additions to binary, hypoeutectic, coarse-grained Al(Sc) alloys (the Al–Sc–Zr phase diagram is shown in Ref. [11]) by examining their ambient temperature mechanical properties (utilizing microhardness measurements), their elevated-temperature mech-

anical properties (in the form of creep properties), and correlating these results to their microstructure (average precipitate radius and volume fraction).

2. Experimental methods

Six Al(Sc,Zr) alloys were produced by melting Al–1.2 at.% Sc and Al–5.0 at.% Zr master alloys with 99.99 at.% pure Al in air. After stirring at 720 °C, the melt was cast into a boron nitride coated graphite mold resting on a large copper plate to encourage directional solidification, which occurred at an estimated rate of $\sim 25 \text{ K s}^{-1}$ [11]. All ingot mass densities were measured to be $99.90 \pm 0.03\%$ of the theoretical density by Archimedes' method.

Table 1 lists the average composition of the Al(Sc,Zr) alloys, determined by chemical mass emission analysis (Galbraith Laboratories, Knoxville, TN and Luvak, Boylston, MA) from samples located near the center of the ingot, and given in the following as at.% unless otherwise noted. Also listed in Table 1 are the Sc/Zr atomic ratios and lattice parameter misfits (at 24 and 300 °C) of the Al(Sc,Zr) alloys, calculated using lattice parameters of 0.40488 nm for Al [21] and 0.4103 nm for Al_3Sc [3]; a change in lattice parameter with Zr addition in $Al_3(Sc,Zr)$ of $8.82 \pm 2.95 \times 10^{-5} \text{ nm at.}^{-1}$ [3]; and a thermal expansion strain between 24 and 300 °C of 0.415% for Al_3Sc [22] and 0.699% for Al [23]. Heat treatments were performed in air in resistively heated furnaces. Homogenization in the single-phase region was performed for the ternary alloys at 648 °C for 72 h, and for the binary alloys at 640 °C for 24 h. After homogenization, samples were water-quenched to 24 °C and aged, within the two-phase region to produce $Al_3(Sc_{1-x}Zr_x)$ precipitates, at temperatures between 300 and 400 °C for times between 0.5 and 288 h (Table 2). Transmission electron microscopy (TEM) samples were produced and analyzed for precipitate radii according to the procedures given in Refs. [10,11].

Creep specimens were machined from heat-treated (homogenized at 648 °C for 72 h and aged at 300 °C for 72 h) ingots into dog-bone shaped tensile bars with a gauge length of 18 mm and a

Table 1
Composition and lattice parameter misfit of alloys investigated

Alloy (at.%)	Sc (wt.%)	Zr (wt.%)	Sc/Zr ratio		Lattice parameter misfit, δ (%)	
			(at./at.%)	(wt./wt.%)	24 °C	300 °C
Al–0.06 Sc–0.005 Zr	0.10	0.018	12	5.5	1.30	1.01
Al–0.07 Sc–0.011 Zr	0.10	0.036	6.4	2.8	1.26	0.98
Al–0.07 Sc–0.019 Zr	0.11	0.060	3.7	1.8	1.22	0.94
Al–0.09 Sc–0.047 Zr	0.15	0.16	1.9	0.94	1.15	0.87
Al–0.14 Sc–0.012 Zr	0.24	0.040	12	6.0	1.30	1.01
Al–0.16 Sc–0.010 Zr	0.27	0.030	16	9.0	1.31	1.02
Al–0.18 Sc	0.3	–	–	–	1.34	1.05

Table 2
Effect of composition and aging treatment upon precipitate volume fraction, V_V , average precipitate radius, $\langle r \rangle$, inter-precipitate spacing, λ , experimental threshold stress, σ_{th} , calculated Orowan stress, σ_{or} , and shearing stress, σ_{sh} . The error represents $\pm \sigma$ values

Alloy (at. %)	Heat treatment	V_V (%) ^a	$\langle r \rangle$ (nm)	λ (nm) ^c	σ_{th} (MPa) ^b	σ_{or} (MPa) ^d	σ_{sh} (MPa) ^e
Al–0.06 Sc–0.005 Zr	300 °C, 72 h	0.31	3.3 ± 0.2	76 ± 4	12	114	220
	300 °C, 5 h + 350 °C, 48 h	0.27	5.9 ± 0.3	155 ± 8	18	68	248
Al–0.07 Sc–0.011 Zr	300 °C, 72 h	0.345	2.7 ± 0.1	62 ± 3	13	132	215
	320 °C, 24 h	0.34	7.6 ± 0.4	176 ± 9	20	64	298
Al–0.07 Sc–0.019 Zr	300 °C, 72 h	0.38	2.3 ± 0.1	50 ± 3	14	153	213
	350 °C, 72 h	0.37	8.7 ± 0.4	193 ± 10	20	60	320
Al–0.09 Sc–0.047 Zr	300 °C, 72 h	0.71	2.0 ± 0.1	31 ± 2	15	234	273
	350 °C, 17 h	0.69	2.7 ± 0.1	43 ± 2	18	192	296
	350 °C, 288 h	0.69	4.8 ± 0.2	76 ± 4	20	130	344
	375 °C, 3 h	0.68	8.1 ± 0.4	129 ± 6	23	89	415
Al–0.14 Sc–0.012 Zr	300 °C, 72 h	0.74	2.4 ± 0.1	36 ± 2	17	214	307
	300 °C, 72 h + 400 °C, 4.75 h	0.70	3.6 ± 0.2	56 ± 3	23	160	340
	300 °C, 72 h	0.77	3.0 ± 0.2	45 ± 2	20	190	338

^a Calculated from thermodynamic data [24] at indicated temperature.

^b Calculated from experimental data at 300 °C.

^c Calculated from Eq. (5).

^d Calculated from Eq. (4) at 300 °C.

^e Calculated from Eqs. (1)–(3) at 300 °C.

gauge radius of 2 mm. Prior to testing, creep specimens were re-homogenized and aged according to the schedule in Table 2. Table 2 lists the precipitate volume fractions, V_V , calculated from the thermodynamic data of Ref. [24]: three of the alloys have the volume fraction $V_V = 0.33 \pm 0.05\%$, and the other three have higher volume fractions, $V_V = 0.73 \pm 0.05\%$. Tensile creep testing was performed

in accordance with ASTM #E139 specifications. Specimens were tested at 300 °C employing constant loads in air in a three-zone resistively heated furnace, with a temperature stability of ± 1 °C, after an 85 min soak at the test temperature. The specimen displacement was recorded through a linear voltage displacement transducer (with 2.5 μm resolution) connected to an extensometer, which

was attached to the gauge length. During creep tests, the strain and strain rate were continuously monitored. At any given stress value, sufficient time was allowed to establish a minimum creep rate. After the minimum creep rate was found, the load was changed (in most cases to a higher value) and the primary and secondary creep rates were again measured at the new stress value. The range of stresses (10–35 MPa) and strain rates (2×10^{-9} – $1 \times 10^{-4} \text{ s}^{-1}$) were selected to ensure that creep deformation occurred by dislocation glide and climb (power-law creep regime).

Vickers microhardness measurements were performed on $1 \times 1 \times 0.3 \text{ cm}^3$ samples from each alloy, which were aged simultaneously to ensure consistent results. A minimum of 20 hardness measurements was performed on each sample, and their statistical scatter determined the measurement error. All of the experimental errors reported here represent one standard deviation from the mean.

3. Results

3.1. Transmission electron microscopy

Directional solidification produces a coarse as-cast grain size ($0.7 \pm 0.1 \text{ grain per mm}^{-2}$), so that grain-boundary strengthening at ambient temperature and grain-boundary creep at elevated temperatures are negligible. Due to the casting procedure, sub-grain boundaries are not observed in undeformed Al(Sc,Zr) TEM specimens. Fig. 1(a–d) are representative TEM images of two Al(Sc,Zr) alloys, which show the fine, coherent $\text{Al}_3(\text{Sc}_{1-x}\text{Zr}_x)$ precipitates that formed upon aging of the supersaturated Al(Sc,Zr) solid solution. Fig. 1(a,b) demonstrate the effect of aging time and temperature on the average precipitate radius, $\langle r \rangle$, and number density, N_V , for the smaller V_V alloy Al–0.07 Sc–0.011 Zr: aging at 300 °C for 72 h produces $\langle r \rangle = 2.7 \pm 0.1 \text{ nm}$ (Fig. 1(a)) and aging at 320 °C for 24 h yields $\langle r \rangle = 7.6 \pm 0.4 \text{ nm}$ (Fig. 1(b)).

Fig. 1(c,d) exhibit similar trends, but for the Al–0.09 Sc–0.047 Zr alloy with a larger V_V : aging at 350 °C for 17 h produces $\langle r \rangle = 2.7 \pm 0.1 \text{ nm}$ (Fig. 1(c)) and aging at 375 °C for 3 h yields $\langle r \rangle = 8.1 \pm 0.4 \text{ nm}$ (Fig. 1(d)). Increasing the aging tem-

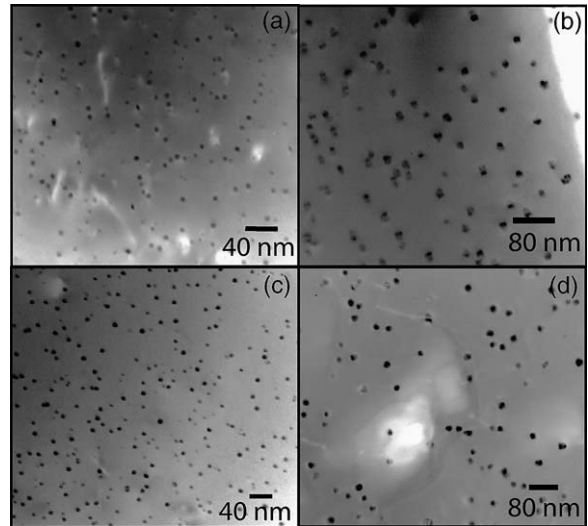


Fig. 1. Comparison of $\text{Al}_3(\text{Sc}_{1-x}\text{Zr}_x)$ precipitates as observed employing superlattice dark-field CTEM images (utilizing 1 0 0 superlattice reflections near the [1 0 0] zone axis) of: (a) a lower V_V alloy Al–0.07 Sc–0.011 Zr aged at 300 °C for 72 h and (b) 320 °C for 24 h; and (c) a higher V_V alloy Al–0.09 Sc–0.047 Zr aged at 350 °C for 17 h and (d) 375 °C for 3 h.

perature by 20–25 K for both alloys nearly triples $\langle r \rangle$, despite a strong decrease in aging time. This increase in $\langle r \rangle$ is associated with a decrease in N_V . A doubling of V_V , however, from 0.35% for Al–0.07 Sc–0.011 Zr to 0.69% for Al–0.09 Sc–0.047 Zr, increases N_V by over a factor of 4—from $(9.0 \pm 2.3) \times 10^{21} \text{ m}^{-3}$ to $(4.0 \pm 1.0) \times 10^{22} \text{ m}^{-3}$ —as illustrated in Fig. 1(a,c).

3.2. Microhardness

Microhardness vs. aging time curves of four Al(Sc) and Al(Sc,Zr) alloys (Fig. 2) exhibit the expected four regions of precipitation-strengthened alloys: (1) incubation; (2) rapid increase in hardness (under-aging); (3) plateau in hardness (peak-aging); and (4) decrease in hardness (over-aging). Fig. 2 demonstrates the variation in Vickers hardness as a function of aging temperature for two ternary alloys, Al–0.14 Sc–0.012 Zr (larger V_V) and Al–0.06 Sc–0.005 Zr (smaller V_V), and their equivalent binary alloys, Al–0.18 Sc and Al–0.07 Sc [5,25], respectively. At constant aging temperature, the incubation and under-aging times

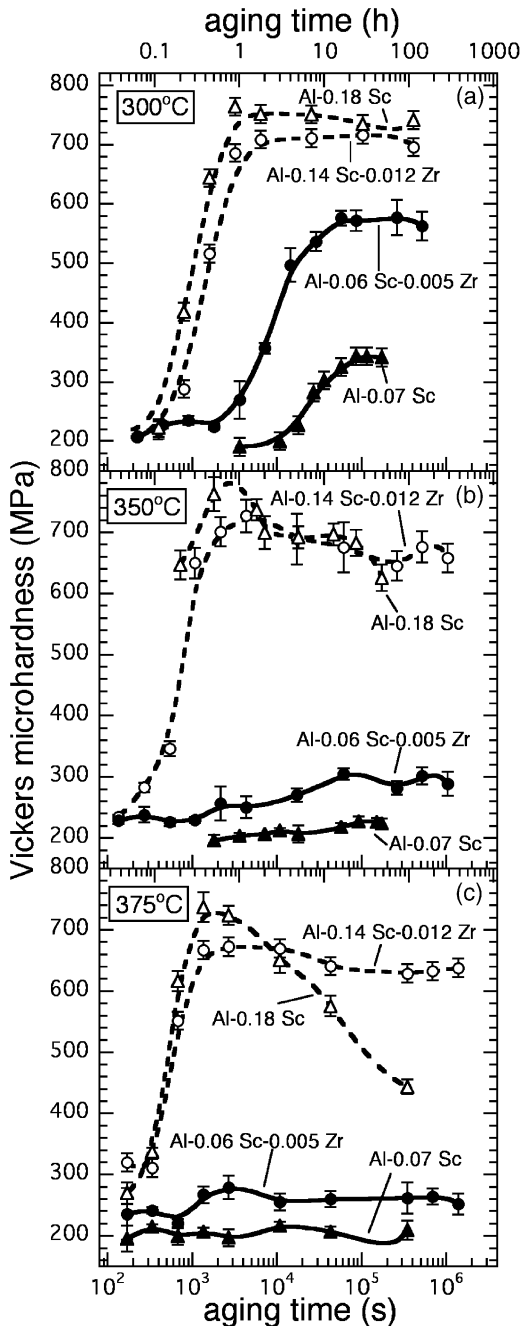


Fig. 2. Vickers microhardness (MPa) vs. aging time at: (a) 300 °C, (b) 350 °C, and (c) 375 °C for two ternary Al(Sc,Zr) alloys and two corresponding binary Al(Sc) alloys. Data from Refs. [5,25] are used for Al(Sc) alloys in (a) and (b).

increase, but the peak hardness decreases with decreasing V_V .

Aging at 300 °C, Fig. 2(a), produces peak hardness values that remain constant for up to 144 h. Thus, the mechanical properties of Al(Sc,Zr) alloys are not expected to change significantly during the creep experiments at 300 °C, which were shorter than 120 h. The peak hardness of the ternary Al-0.06 Sc-0.005 Zr alloy is substantially higher than the binary Al-0.07 Sc alloy, while both alloys have similar precipitate volume fractions (0.31% for Al-0.06 Sc-0.005 Zr and 0.23% for Al-0.07 Sc [5]). This difference can be attributed to the ternary alloy containing smaller precipitates ($\langle r \rangle = 3.3$ nm) than the binary alloy ($\langle r \rangle = 8.5$ nm [5]) after aging at 300 °C for 72 h.

The microhardness curves of the larger V_V alloys, Al-0.14 Sc-0.012 Zr and Al-0.18 Sc, demonstrate that an increase in the aging temperature (from 300 to 350 and 375 °C, Fig. 2(a–c)) results in a decrease in the incubation time, duration of under-aging, and peak hardness value and duration. Zirconium additions increase the duration of peak hardness when alloys are aged at 350 and 375 °C. This is especially apparent at 375 °C (Fig. 2(c)), where rapid over-aging of the Al-0.18 Sc alloy is observed after less than 1 h, while the Al-0.14 Sc-0.012 Zr alloy exhibits only a slight over-aging at 384 h.

Aging at 350 and 375 °C dramatically reduces the strength of the smaller V_V alloys, Al-0.06 Sc-0.005 Zr and Al-0.07 Sc, as compared to aging at 300 °C; this is due to the large average radius of the precipitates ($\langle r \rangle$ larger than 10 nm [10]), which do not provide a significant contribution to alloy strengthening. At all temperatures, the ternary alloy has higher hardness values than the binary alloy, which is due to the ternary alloy containing smaller precipitates [10].

3.3. Creep properties

Creep behavior at 300 °C is illustrated in Fig. 3 for two smaller V_V alloys (Al-0.06 Sc-0.005 Zr and Al-0.07 Sc-0.019 Zr) and two larger V_V alloys (Al-0.09 Sc-0.047 Zr and Al-0.14 Sc-0.012 Zr), all aged at 300 °C for 72 h. Creep resistance is observed to increase with increasing V_V at approxi-

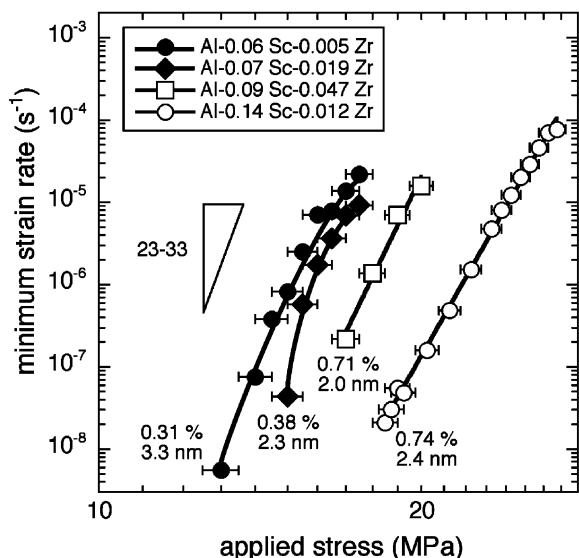


Fig. 3. Double logarithmic plot of minimum creep rate at 300 °C vs. applied stress, for Al(Sc,Zr) alloys with various precipitate volume fractions V_v (given in %) and roughly constant precipitate radius $\langle r \rangle$ (given in nm). All alloys were aged at 300 °C for 72 h.

mately constant $\langle r \rangle$ (2.0–3.1 nm). In addition, the stress exponents of the ternary alloys (slopes of lines, $n = 23$ –33 in Fig. 3) are much greater than that of annealed Al ($n = 4.4$ [26]), indicating the presence of a threshold stress. The threshold stress, σ_{th} , is found by plotting the strain rate raised to the power $1/4.4$ as a function of stress, following the procedure of Ref. [27]. Values for σ_{th} at 300 °C vary between 12 and 23 MPa (Table 2) for all of the tested Al(Sc,Zr) alloys.

Creep testing of the larger V_v (Al–0.09 Sc–0.047 Zr) alloy (Fig. 4) shows that an increase in creep resistance is caused by an increase in $\langle r \rangle$ from 2.0 to 8.1 nm at approximately constant V_v . The effect of Zr additions on the creep resistance of Al(Sc) alloys is further illustrated in Fig. 5, where the creep behaviors of the ternary Al–0.14 Sc–0.012 Zr and Al–0.16 Sc–0.010 Zr alloys are compared to the binary Al–0.18 Sc alloy [5]; all three alloys have similar V_v values. As also demonstrated for the Al–0.09 Sc–0.047 Zr alloy in Fig. 4, the Al–0.14 Sc–0.012 Zr and Al–0.18 Sc alloys exhibit an increase in creep resistance with increasing $\langle r \rangle$ from 2.4 to 3.6 nm for the ternary alloy and from

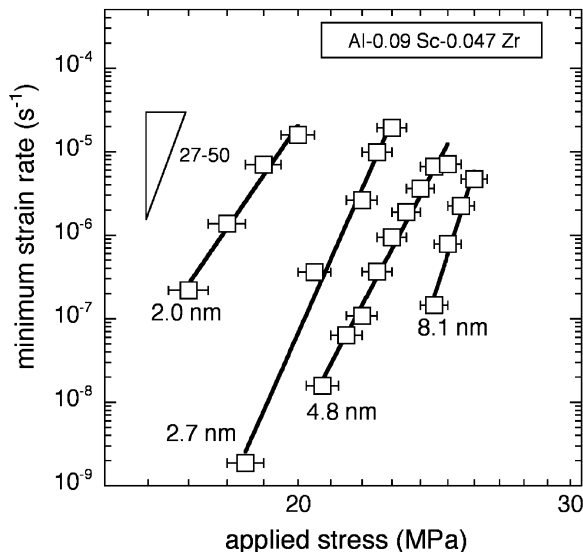


Fig. 4. Double logarithmic plot of minimum creep rate at 300 °C vs. applied stress for a higher V_v alloy (Al–0.09 Sc–0.047 Zr) with various precipitate radius $\langle r \rangle$ (given in nm).

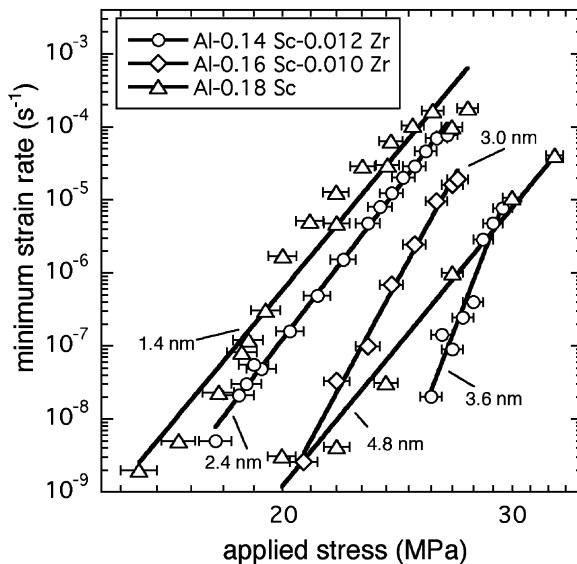


Fig. 5. Double logarithmic plot of minimum creep rate at 300 °C vs. applied stress for the higher V_v alloys Al–0.14 Sc–0.012 Zr and Al–0.16 Sc–0.010 Zr and the corresponding binary Al–0.18 Sc alloy with various precipitate radius $\langle r \rangle$ (given in nm).

1.4 to 4.8 nm for the binary alloy. While the values of $\langle r \rangle$ are not exactly the same for the binary and ternary alloys Fig. 5, they are close enough that a comparison of creep resistance among the three alloys can be made. At the smallest precipitate radius, the creep resistance of the Al–0.18 Sc alloy ($\langle r \rangle = 1.4 \pm 0.1$ nm) is slightly smaller than that of the Al–0.14 Sc–0.012 Zr alloy ($\langle r \rangle = 2.4 \pm 0.1$ nm). At the larger values of precipitate radii ($\langle r \rangle \geq 3.0$), the differences in stress sensitivity (different slopes) and precipitate radii makes a detailed comparison difficult, but the binary alloy has approximately the same threshold stress as the ternary alloys.

4. Discussion

4.1. Transmission electron microscopy

Zirconium additions decrease the rate of precipitate coarsening as observed in Fig. 2 and reported in Ref. [10], such that creep tests at 300 °C lasting over a week can be performed on ternary Al(Sc,Zr) alloys without significant precipitate coarsening. High-resolution electron microscopy (HREM) of the Al(Sc,Zr) alloys aged at 300 °C for 576 h show $\text{Al}_3(\text{Sc,Zr})$ precipitates to have facets parallel to the $\{100\}$ and $\{110\}$ planes [10,11], which were less well defined than in binary Al(Sc) [28].

4.2. Microhardness

Fig. 6 compares the increment in yield strength as a function of $\langle r \rangle$, measured in Ref. [10] for two smaller V_V alloys (Al–0.06 Sc–0.005 Zr and Al–0.07 Sc–0.019 Zr) with similar precipitate volume fractions, which do not significantly change between 300 and 375 °C (Table 2). The increment in yield strength was determined by subtracting the as-homogenized hardness from the as-aged hardness and dividing the result by 2.8, a conversion factor valid for Al alloys [29], but not for pure Al. Compressive yield strength measurements of Al(Sc) alloys have shown this approximation to be accurate in predicting alloy strengthening [5]. Experimentally, the maximum increment of strength (≈ 140 MPa) occurs at the lowest values

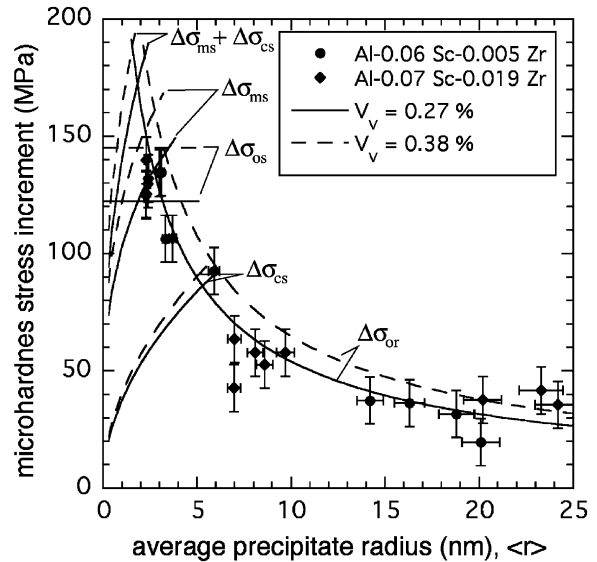


Fig. 6. Microhardness yield stress increment vs. average precipitate radius $\langle r \rangle$ for the lower V_V alloys: Al–0.06 Sc–0.005 Zr ($V_V=0.27\text{--}0.31\%$) and Al–0.07 Sc–0.019 Zr ($V_V=0.37\text{--}0.38\%$). The lines represent predictions of Eqs. (1)–(5) for $V_V=0.27$ and 0.38%.

of $\langle r \rangle$ (ca. 2.5 nm) and decreases with increasing $\langle r \rangle$, as expected if the Orowan dislocation looping mechanism is dominant. The same trends are displayed in Fig. 7 for two of the larger V_V alloys (Al–0.09 Sc–0.047 Zr and Al–0.14 Sc–0.012 Zr), which have similar precipitate volume fractions between 300 and 375 °C (Table 2). The precipitates in these two larger V_V alloys coarsen at a slower rate than the precipitates in the smaller V_V alloys shown in Fig. 6 [10], so the maximum values of $\langle r \rangle$ are smaller (10.5 vs. 24 nm). A similar behavior was observed for the increment in yield strength of a binary Al–0.18 at.% Sc alloy [5] with a maximum increment of strength ≈ 180 MPa at $\langle r \rangle = 2\text{--}3$ nm, decreasing monotonically with increasing $\langle r \rangle$, and therefore a similar discussion applies, as outlined below.

Precipitate shearing, precipitate bypass by dislocation looping, or a combination of these two mechanisms can generally explain ambient temperature strength in coarse-grained, non-strain-hardened, precipitation-strengthened alloys [30]. Deformation by dislocation shearing is expected to occur at small $\langle r \rangle$ and three mechanisms have been

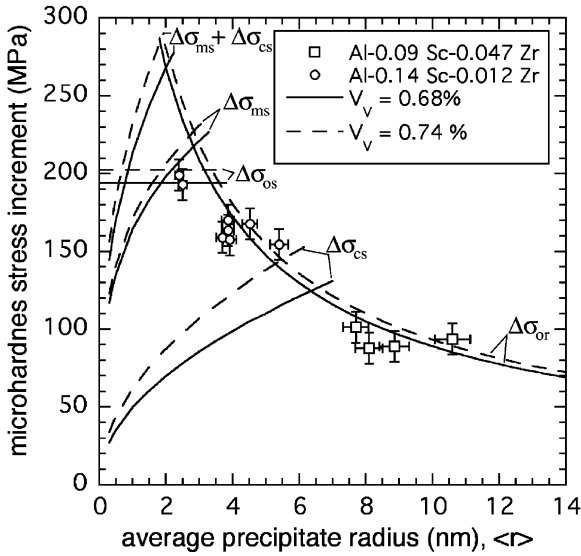


Fig. 7. Microhardness yield stress increment vs. average precipitate radius $\langle r \rangle$ for the higher V_v alloys: Al-0.09 Sc-0.047 Zr ($V_v=0.68\text{--}0.71\%$) and Al-0.14 Sc-0.012 Zr ($V_v=0.70\text{--}0.74\%$). The lines represent predictions of Eqs. (1)–(5) for $V_v=0.68$ and 0.74% .

postulated to explain this process: (i) modulus hardening; (ii) coherency strengthening; and (iii) order strengthening. The strength increment due to modulus strengthening, $\Delta\sigma_{ms}$, is caused by the mismatch between the shear moduli of the precipitate and matrix phases and is given by [30]:

$$\Delta\sigma_{ms} = M0.0055(\Delta G)^{3/2} \left(\frac{2V_v}{Gb^2} \right)^{1/2} b \left(\frac{\langle r \rangle}{b} \right)^{(3m/2)-1}; \quad (1)$$

where $M = 3.06$ is the matrix orientation factor [31], G is the shear modulus of Al (25.4 GPa at 24 °C [26]), ΔG is the modulus mismatch between Al and the $\text{Al}_3(\text{Sc,Zr})$ precipitates (assumed to have the same stiffness, 68 GPa, as Al_3Sc [32]), b is the magnitude of the Burgers vector of Al (0.286 nm [26]), and $m = 0.85$ is a constant [30].

Coherency strengthening is due to strain–field interactions between a coherent precipitate and a dislocation. The strength increment due to coherency strengthening, $\Delta\sigma_{cs}$, is given by [30]:

$$\Delta\sigma_{cs} = \chi M(\varepsilon G)^{3/2} \left(\frac{\langle r \rangle V_v}{0.18Gb} \right)^{1/2}; \quad (2)$$

where $\chi = 2.6$ is a constant [30], ε is the lattice parameter misfit, $\varepsilon \approx (2/3)\delta$, with $\delta = \Delta a/a$ as the ambient temperature lattice parameter misfit (Table 1).

Finally, order strengthening is due to the formation of an antiphase boundary (APB), which occurs when a matrix dislocation shears an ordered precipitate. The strength increment due to order strengthening, $\Delta\sigma_{os}$, is given by [30]:

$$\Delta\sigma_{os} = M0.81 \frac{\gamma_{apb}}{2b} \left(\frac{3\pi V_v}{8} \right)^{1/2}; \quad (3)$$

where γ_{apb} is the APB energy of the precipitate phase (assumed to be equal to the average value for Al_3Sc , 0.5 J m^{-2} [33,34]).

Alternatively, precipitate bypass can occur through the Orowan mechanism by dislocation looping around the precipitates. The corresponding Orowan stress, $\Delta\sigma_{or}$, is [35]:

$$\Delta\sigma_{or} = M \frac{0.4Gb \ln(2\bar{r}/b)}{\pi\lambda \sqrt{1-\nu}}; \quad (4)$$

where $\nu = 0.345$ is Poisson's ratio of Al [31], $\bar{r} = \sqrt{2/3} \langle r \rangle$ is the mean radius of a circular cross-section in a random plane for a spherical precipitate [35], and λ is the inter-precipitate spacing. The latter parameter is calculated assuming that spherical precipitates are arranged on a cubic grid (which is a valid simplification for the small V_v values in this study) [36]:

$$\lambda = 2\bar{r} \left(\sqrt{\frac{\pi}{4V_v}} - 1 \right). \quad (5)$$

Utilizing Eqs. (1)–(5), the ambient temperature yield stress increment due to the presence of $\text{Al}_3(\text{Sc,Zr})$ precipitates is calculated, as shown in Figs. 6 and 7. The calculated predictions are compared to the experimental data for the ternary Al(Sc,Zr) alloys.

As suggested in Ref. [5], the increment in strengthening due to shearing of precipitates is taken as the larger of (a) the sum of modulus strengthening and coherency strengthening ($\sigma_{ms}+\sigma_{cs}$), or (b) the order strengthening, σ_{os} . This is because these two mechanisms (a,b) are sequen-

tial, the former occurring before the dislocation shears the precipitate and the latter during shearing. Because the shearing and bypassing mechanisms are in parallel, strengthening is given by the smallest of these strengthening modes. Fig. 6 thus predicts that $\Delta\sigma_{os}$ is dominant for $\langle r \rangle$ less than 0.5 nm, ($\Delta\sigma_{ms} + \Delta\sigma_{cs}$) for $\langle r \rangle$ between 0.5 and 2.0 nm, and $\Delta\sigma_{or}$ for $\langle r \rangle$ larger than 2.0 nm. All alloys have $\langle r \rangle$ larger than 2.0 nm and their strength is thus predicted to be controlled by the Orowan mechanism. Fig. 6 shows good quantitative agreement between experimental data and the $\Delta\sigma_{or}$ value predicted by Eq. (4) for the present range of V_V values, as also observed for Al–0.18 at.% Sc in Ref. [5]. Fig. 7 indicates that the same prediction (Orowan bypassing is the controlling mechanism for $\langle r \rangle$ larger than 2.0 nm) applies to the larger V_V alloys (Al–0.09 Sc–0.047 Zr and Al–0.14 Sc–0.012 Zr), and the experimental data is again in good quantitative agreement with this prediction. Figs. 6 and 7 indicate that significant increases in strength can be achieved by a small decrease in $\langle r \rangle$ to the optimal value of 2.0 nm, which is achievable through aging treatments below 300 °C.

Compared to the binary Al(Sc) alloy, ternary alloying additions can affect the lattice parameter misfit, the APB energy, and the elastic modulus, thus changing $\Delta\sigma_{ms}$, $\Delta\sigma_{cs}$, and $\Delta\sigma_{os}$. Zirconium additions should slightly decrease $\Delta\sigma_{cs}$ by decreasing the lattice parameter misfit (Table 1). Zirconium is, however, not expected to have a significant effect on the modulus of the precipitate phase, so the value of $\Delta\sigma_{ms}$ should not change. The value of $\Delta\sigma_{os}$ is expected to increase due to an increase in the APB energy of the precipitate phase, as indicated by an increase in the creep resistance of $Al_3(Sc_{0.74}Zr_{0.26})$ with respect to Al_3Sc [20]. Literature values for the APB energy of $Al_3(Sc,Zr)$ do not exist, however, so the degree of the increase in the ordering contribution cannot be assessed. The combination of these three shearing mechanisms indicates that Zr additions should slightly increase the total increment of shearing, so the calculated curves shown in Figs. 6 and 7 should be considered as lower bounds. However, $\Delta\sigma_{or}$ is unaffected by Zr additions, and all of the experimental data is in the regime $\langle r \rangle > 2.0$ nm, where the Orowan mechanism is controlling.

4.3. Creep properties

When deformation is controlled by dislocation climb, the creep behavior of precipitation- or dispersion-strengthened materials follows a power-law equation generally represented by:

$$\dot{\epsilon} = A_{ap}\sigma^{n_{ap}}\exp\left(\frac{-Q_{ap}}{RT}\right); \quad (6)$$

where $\dot{\epsilon}$ is the strain rate, A_{ap} is a constant, σ is the applied stress, n_{ap} is the apparent stress exponent, Q_{ap} is the apparent activation energy, and R and T have their usual significance. When the apparent stress exponent is much higher than that of the matrix (i.e. $n_{ap} > 10$), an athermal threshold stress, σ_{th} , is assumed, below which creep is not measurable in the laboratory [37]. This leads to a modified power-law equation:

$$\dot{\epsilon} = A[\sigma - \sigma_{th}]^n \exp\left(\frac{-Q}{RT}\right); \quad (7)$$

where A is a constant, n is the matrix stress exponent, and Q is the matrix creep activation energy, which is usually equal to the activation energy for volume self-diffusion. The rationale for the existence of a threshold stress is that matrix dislocations require some minimum amount of energy through the applied stress to bypass the second-phase precipitates [38].

Large threshold stresses are typically associated with incoherent dispersoids or precipitates [37–41]. Threshold stress behavior has been, however, observed in two alloys containing coherent $L1_2$ precipitates as in the present Al(Sc,Zr) alloys: a rapidly solidified Al–V–Zr alloy tested at 425 °C, containing $Al_3(Zr,V)$ precipitates ($V_V = 5.0\%$, $\langle r \rangle \leq 5$ nm) [42], and in binary Al(Sc) alloys tested at 300 °C, containing Al_3Sc precipitates ($V_V = 0.24–0.71\%$, $\langle r \rangle = 1.4–9.6$ nm) [5].

The threshold stress is due to dislocations bypassing precipitates by shearing them or climbing over them. If shearing is the operating threshold stress mechanism in the Al(Sc,Zr) alloys, σ_{th} must equal to σ_{sh} , where σ_{sh} is taken as the larger of $(\sigma_{ms} + \sigma_{cs})$ or σ_{os} , as discussed in Section 4.2. Table 2 shows the calculated values of σ_{sh} at 300 °C to be much greater than the experimental values

of σ_{th} (by a factor 15–18), thus shearing cannot be the operating mechanism.

In climb-controlled bypass, the threshold stress is due to an increase in the line length of dislocations during the climb process [38]. The accepted mechanism by which dislocations change their line length is general climb, σ_{gen} :

$$\sigma_{gen} = 0.8\kappa\sigma_{or}; \quad (8)$$

where κ is a function of the particle volume fraction, as given by McLean [39]. In general climb, dislocations experience a small increase in dislocation length in order for the dislocation to climb over precipitates, which leads to small threshold stress values on the order of $0.02\sigma_{or}$.

An increase in the creep resistance with an increase in V_v , as shown in Fig. 3, is anticipated, because, as V_v increases, the inter-precipitate distance decreases (Eq. (5)), which produces an increase in the Orowan and threshold stresses (Eqs. (4) and (8)). An increase in the creep resistance with an increase in $\langle r \rangle$ (Figs. 4 and 5) is, however, contrary to the predictions of Eqs. (4) and (8). Such an increase was also observed for binary Al(Sc) alloys [5] and is discussed here along the same lines.

Determination of the operating climb mechanism is accomplished by utilizing Eqs. (4) and (5) to determine the inter-precipitate spacing, λ , and σ_{or} (Table 2), which are compared to the measured σ_{th} displayed in Table 2. From Table 2, a plot of σ_{th}/σ_{or} (normalized threshold stress) as a function of $\langle r \rangle$ is produced (Fig. 8). The normalized threshold stress removes the dependency on V_v , so the data for all ternary alloys can be plotted on the same graph. For comparison, the creep threshold data for the binary Al–0.07 Sc, Al–0.12 Sc, and Al–0.18 Sc (at.%) alloys [5] are also plotted in Fig. 8. The experimental values of normalized threshold stress are observed to increase with increasing $\langle r \rangle$, which does not follow the radius-independent prediction of the general climb model, Eq. (8).

The $\langle r \rangle$ dependence of the normalized threshold stress in Al(Sc,Zr) alloys can be compared to a model recently developed for creep of alloys containing coherent precipitates [43], whose predictions are shown by the solid curves in Fig. 8. This model assumes that dislocations are subjected to

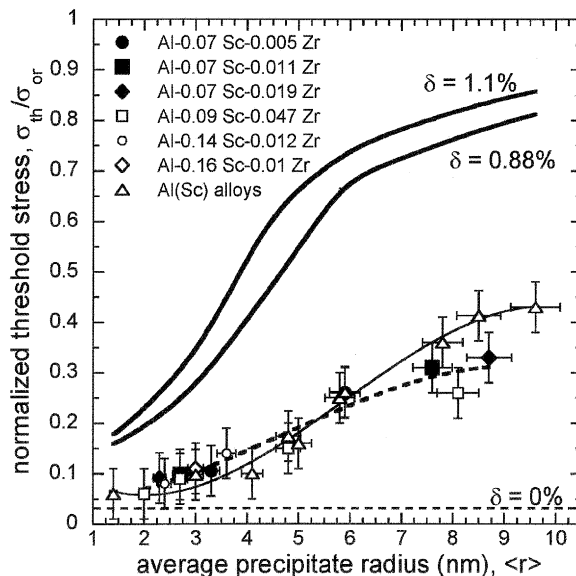


Fig. 8. Threshold stress normalized by Orowan stress at 300 °C (σ_{th}/σ_{or}) vs. average precipitate radius $\langle r \rangle$ for ternary Al(Sc,Zr) alloys (lattice misfit $\delta = 0.87$ – 1.02%) and binary Al–0.07 Sc, Al–0.12 Sc, and Al–0.18 Sc alloys ($\delta = 1.05\%$) [5]. The lines represent predictions from a recently proposed model [43] considering elastic interactions between dislocations and coherent precipitates ($\delta = 0.8$ and 1.1%). Also shown is the general climb model without elastic interactions ($\delta = 0$).

elastic stresses from the modulus and lattice parameter misfits between the matrix and precipitate phases. Both the present Al(Sc,Zr) alloys, and the previously investigated Al(Sc) alloys [5] follow the general trend of this model. At small values of $\langle r \rangle$, the Al(Sc) and Al(Sc,Zr) data overlap. At values of $\langle r \rangle$ greater than 7 nm, the threshold stress values of the Al(Sc) and Al(Sc,Zr) alloys are within one standard deviation of each other, but the three data points for the ternary Al(Sc,Zr) alloys exhibit lower normalized threshold stresses than the three corresponding binary Al(Sc) data points. This model indeed predicts the trend of smaller threshold stresses for ternary Al(Sc,Zr) alloys as compared to the binary alloy, illustrated by the two curves with different lattice parameter mismatches (Fig. 8). With a smaller lattice parameter misfit, the elastic interaction between the precipitate and dislocation is reduced and the strengthening effect is decreased. The effect of the

lattice parameter misfit is enhanced at large $\langle r \rangle$, since the interaction volume increases with $\langle r \rangle^3$.

The chemical composition of Al_3Sc precipitates is anticipated to change with Zr additions, due to Zr enrichment near the precipitate/matrix heterophase interface [11,44], which could alter the precipitate/dislocation interaction, e.g. by further modifying the misfit. Large differences were not, however, observed between the creep behavior of the $\text{Al}(\text{Sc})$ and $\text{Al}(\text{Sc},\text{Zr})$ alloys with the same precipitate volume fraction and average radius (Fig. 8), indicating that the above chemical effect has a small impact on creep resistance. A three-dimensional atom probe examination of the $\text{Al}-0.09 \text{Zr}-0.047 \text{Zr}$ alloy aged at 300°C indicated that, after aging at 300°C for 2412 h, the $\text{Al}_3(\text{Sc}_{1-x}\text{Zr}_x)$ precipitates are not in global thermodynamic equilibrium [11]. It is proposed that $\text{Al}(\text{Sc},\text{Zr})$ alloys will not reach a global equilibrium, within reasonable time periods, when aged between 300 and 375°C . Thus, a chemical effect upon the creep resistance of $\text{Al}(\text{Sc},\text{Zr})$ alloys is more likely to occur at aging temperatures above 375°C , if it exists at all.

The optimum $\langle r \rangle$ value depends on the intended use of an alloy. At ambient temperature, as illustrated in Figs. 6 and 7, the optimal strength is achieved with $\langle r \rangle = 2.0 \text{ nm}$. At 300°C , however, Fig. 8 shows that optimal dislocation creep resistance occurs at the largest value of $\langle r \rangle$, 8.7 nm . As the Orowan stress decreases, however, with increasing $\langle r \rangle$, the magnitude of the threshold stress increases only modestly in the range $\langle r \rangle = 4\text{--}9 \text{ nm}$ (Table 2). A compromise $\langle r \rangle$ value for an alloy needing strength both at ambient and elevated temperature is then ca. 4 nm . Solute atoms and embryonic particles of the Al_3Sc phase may affect the ambient- and elevated-temperature strengths of the alloys studied [45]; however, because the number density and size of these embryos are not known and would be very difficult to ascertain, we do not attempt here to calculate whether they will make a significant contribution to the mechanical properties of the alloys.

5. Conclusions

The following conclusions are drawn from this study of the ambient- and elevated-temperature mechanical properties of six $\text{Al}(\text{Sc},\text{Zr})$ alloys:

- Microhardness increases with increasing precipitate volume fraction (Fig. 2), and with decreasing average precipitate radius $\langle r \rangle$ (Figs. 6 and 7). The $\text{Al}-0.14 \text{Sc}-0.12 \text{Zr}$ and $\text{Al}-0.06 \text{Sc}-0.005 \text{Zr}$ alloys maintain their peak hardness for aging times as long as 144 h, at 300°C , Fig. 2(a). Upon aging at 350 and 375°C , the onset and speed of over-aging are delayed for the ternary $\text{Al}-0.14 \text{Sc}-0.012 \text{Zr}$ alloy, as compared to the binary $\text{Al}-0.18 \text{Sc}$ (Fig. 2(b,c)), which is attributed to the slower coarsening kinetics of the Zr-containing alloy. Strength (calculated from microhardness) decreases with increasing $\langle r \rangle$ in good quantitative agreement with predictions assuming the Orowan dislocation looping mechanism for $\langle r \rangle$ larger than 2 nm (Figs. 6 and 7).
- Creep resistance at 300°C increases with increasing volume fraction (Fig. 3) and precipitate radius (Figs. 4 and 5). All alloys exhibit a threshold stress, which increases from $0.06\sigma_{\text{or}}$ at $\langle r \rangle = 2.0 \text{ nm}$ to $0.33\sigma_{\text{or}}$ at $\langle r \rangle = 8.7 \text{ nm}$ (Table 2), where σ_{or} is the Orowan stress. These high relative values of the threshold stress can be semi-quantitatively explained by a recently proposed model [43], taking into account the elastic interactions occurring between dislocations and precipitates, Fig. 8. At the largest values of $\langle r \rangle$ (above 7 nm), Zr additions lead to a slight decrease in creep resistance as compared to binary $\text{Al}(\text{Sc})$ alloys, which can be explained by a decrease in the lattice misfit strain energy, thereby decreasing the dislocation–precipitate interaction.
- At ambient temperature, the maximum alloy strength is predicted at the transition from precipitate shearing to Orowan bypass at $\langle r \rangle \approx 2.0 \text{ nm}$; while at an elevated temperature (300°C), the maximum creep resistance is reached at $\langle r \rangle \approx 4\text{--}9 \text{ nm}$. Therefore, the optimum precipitate radius depends on the usage temperature, and is a compromise between these two values.

Acknowledgements

This research was supported by the United States Department of Energy, Basic Energy

Sciences Division, under contract DE-FG02-98ER45721. The authors thank Dr. E.A. Marquis (Northwestern University) for calculating curves in Fig. 8, as well as Dr. R.W. Hyland, Jr. and Dr. J.L. Murray (Alcoa Inc.) for useful discussions. We would also like to thank Alcoa Inc. and Ashurst Inc. for supplying the Al–Sc master alloys and Alcoa Inc. for supplying the Al–Zr master alloy.

References

- [1] Okamoto H. *J Phase Equil* 1991;12:612.
- [2] Hyland RW. *Metall Trans* 1992;23A:1947.
- [3] Harada Y, Dunand DC. *Mat Sci Eng A* 2002;329-331:686.
- [4] Fuller CB, Seidman DN, Dunand DC. *Scripta Met* 1999;40:691.
- [5] Marquis EA, Seidman DN, Dunand DC. *Acta Mater* 2002;50:4021.
- [6] Fuller CB. Ph.D. Thesis, Northwestern University, 2003.
- [7] Marquis EA. Ph.D. Thesis, Northwestern University, 2002.
- [8] Elagin VI, Zakharov VV, Pavlenko SG, Rostova TD. *Phys Met Metall* 1985;60:88.
- [9] Toropova LS, Eskin DG, Kharakterova ML, Dobatkina TV. *Advanced aluminum alloys containing scandium—structure and properties*. Moscow, Russia: Gordon and Breach Science Publishers, 1998.
- [10] Fuller CB, Murray JL, Seidman DN. In preparation.
- [11] Fuller CB, Seidman DN. In preparation.
- [12] Toropova LS, Kamardinkin AN, Kindzhibalo VV, Tyvanchuk AT. *Phys Met Metall* 1990;70:106.
- [13] Elagin VI, Zakharov VV, Rostova TD. *Metal Heat Treat Metals* 1992;1:37.
- [14] Davydov VG, Elagin VI, Zakharov VV, Rostova TD. *Metal Sci Heat Treat* 1996;38:347.
- [15] Kun Y, Songrui L, Wenxian L, Yude X. *Trans Nonfer Met Soc China* 1999;9:593.
- [16] Carroll MC, Mills MJ, Daehn GS, Gouma PI, Savage MF, Dunbar BR. In: Das S, editor. *Automotive alloys 1999*. Warrendale, PA: TMS; 2000. p. 239.
- [17] Fuller CB, Krause AR, Dunand DC, Seidman DN. *Mat Sci Eng A* 2002;338:8.
- [18] Diskin AM, Alalykin AA. *Izv Vyssh Uchebn Zaved, Tsvetn Metall* 1991;3:107.
- [19] Chakrabarti DJ. In: Ghosh AK, Bieler TR, editors. *Superplasticity and superplastic forming 1998*. Metals Park, PA: TMS; 1998. p. 155.
- [20] Harada Y, Dunand DC. *Acta Metall* 2000;48:3477.
- [21] JCPDS—International Center for Diffraction Data, 1998.
- [22] Harada Y, Dunand DC. *Scripta Mater*, 2003;48:219.
- [23] Touloukian YS, Kirby RK, Taylor RE, Desai PD. In: *Thermophysical properties of high temperature solid materials*. New York: Macmillan; 1967. p. 2.
- [24] Murray JL. Personal communication. June, 2001.
- [25] Marquis EA, Dunand DC. Unpublished results.
- [26] Frost HJ, Ashby MF. In: *Deformation-mechanism maps: the plasticity and creep of metals and ceramics*. Oxford, UK: Pergamon Press; 1982. p. 26.
- [27] Lagneborg R, Bergman B. *Metal Sci* 1976;10:20.
- [28] Marquis EA, Seidman DN. *Acta Mater* 2001;49:1909.
- [29] Tabor D. *Br J App Phys* 1956;7:159.
- [30] Ardell AJ. *Met Trans A* 1985;16A:2131.
- [31] Meyers MA, Chawla KK. *Mechanical metallurgy: principles and applications*. Paramus, NJ: Englewood Cliffs, 1984.
- [32] Hyland RW, Stiffler RC. *Scripta Metall Mater* 1991;25:473.
- [33] George EP, Horton JA, Porter WD, Schneibel JH. *J Mater Res* 1990;5:1639.
- [34] Fu CL. *J Mater Res* 1990;5:971.
- [35] Hirsch PB, Humphreys FJ. In: Argon A, editor. *The physics and strength of plasticity*. Cambridge, MA: MIT Press; 1969. p. 189.
- [36] Brown LM, Ham RK. In: Kelly A, Nicholson RB, editors. *Strengthening methods in crystals*. Amsterdam: Elsevier; 1971. p. 9.
- [37] Arzt E. *Res Mechanica* 1991;31:399.
- [38] Arzt E. In: Ochiai S, editor. *Mechanical properties of metallic composites*. New York: Marcel Dekker, Inc; 1994. p. 205.
- [39] McLean M. *Acta Metall* 1985;33:545.
- [40] Arzt E, Wilkinson DS. *Acta Metall* 1986;34:1893.
- [41] Rösler J, Arzt E. *Acta Metall* 1990;38:671.
- [42] Chen YC, Fine ME, Weertman JR. *Acta Metall Mater* 1990;38:771.
- [43] Marquis EA, Dunand DC. *Scripta Met* 2002;47:503.
- [44] Vetrano JS, Henager CH. *Micros Microa* 1999;160.
- [45] Nembach E. In: *Particle strengthening of metals and alloys*. Boston, MA: John Wiley and Sons, Inc; 1997. p. 63–144.